Predicting fugitive gas emissions from gob-to-face in longwall coal mines: Coupled analytical and numerical modeling

Ang Liu [a], Shimin Liu [a,*], Gang Wang [b], Derek Elsworth [a]

[a] Department of Energy and Mineral Engineering, G3 Center and Energy Institute, The Pennsylvania State University, University Park, PA 16802, USA
[b] Shandong University of Science and Technology, Mine Disaster Prevention and Control-Ministry of State Key Laboratory Breeding Base, Qingdao 266590, PR China

ARTICLE INFO

ABSTRACT

Understanding gas emission and transport from the gob to the active working face in longwall coal mines is necessary for mine ventilation and gas control planning and optimization. We document a mine-wide ventilation pressure and flow rate survey (p-Q survey) to establish a ventilation network model – including methane gas concentrations recorded at selected face locations. We propose an analytical pressure gradient model to evaluate gob gas emission and its interaction with the ventilation system. This model combines viscous energy losses along a tortuous gas flow path within the gob materials with kinetic energy losses at irregular cross-sections. A numerical gas emission model was also established to predict gas emission rates at the longwall face and to dynamically determine the gas emission rate from the compacted gob. Field monitoring indicates that steady methane concentrations increase monotonically and almost linearly from headgate to tailgate. The average methane emission rates are estimated as 0.0061 m^3/s, 0.0044 m^3/s and 0.00215 m^3/s for wide, intermediate-width and narrow panels. A numerical network model of the mine was validated then calibrated against the field methane monitoring results at our partner mine. We observe that gob compaction and related porosity reduction significantly affects gas emission rate. An eleven-fold increase in stress (1.70–18.68 MPa) results in a nonlinear decrease in porosity of only ∼75% (from 0.368 to 0.093) but a 56-fold reduction on gas emission rate (compared to the maximum transient gas emission rate). The mine-wide ventilation system is especially sensitive to methane emission rates – a 50% increase in emission rate (from 0.00455 m^3/s to 0.00637 m^3/s) clearly impacts concentrations in the return branches. Peak methane concentration at related branches increase 39.7%, from 2.24% to 3.13% with the potential to trigger elevated methane alarms. These results can ultimately provide the data for analyzing the interactions between the caved gob and the ventilation system and define mitigation strategies to minimize gas concentrations and hazard.

© 2020 Elsevier Ltd. All rights reserved.

1. Introduction

Longwall top-coal caving (LTCC) is a highly efficient and economically favorable mining method for thick and ultra-thick coal seams [1–3]. This highly productive technique is believed to be rooted from the original method of soutirage mining developed in France during the 1960s [4]. Following the success of the first LTCC mining panel at the Puhe coal mine in Shenyang in 1984 [5], the LTCC mining method has been broadly deployed for the recovery of thick coal seams. With continuous improvement and modifications, LTCC mining is currently the preferred method for the mining of deep and thick coal seams in China [3]. As shown in Fig. 1, the current LTCC method exerts its unique advantages by dividing the thick or ultra-thick coal seam into two seam-parallel slices, comprising lower and upper sub-layers [6–8]. The lower sub-layer is mechanically cut by the longwall shearer liberating the upper sub-layer to collapse under the combined impact of gravity and overburden pressure. Two conveyors simultaneous collect the broken coal as shown in Fig. 1. In a typical longwall system, the conveyor beneath the shields is used to collect the coal cut by the longwall shearer. Unique to LTCC, is the provision of a behind-shield rear conveyor that continuously transports coal from the top-caving layer [3,9,10]. The LTCC panel advances incrementally as the coal is continuously extracted [11]. The unsupported coal roof behind the hydraulic shields may hang for some time before caving and breaking into caved coal blocks. The large blocks fall into the caved zone and create viable pathways for airflow and the
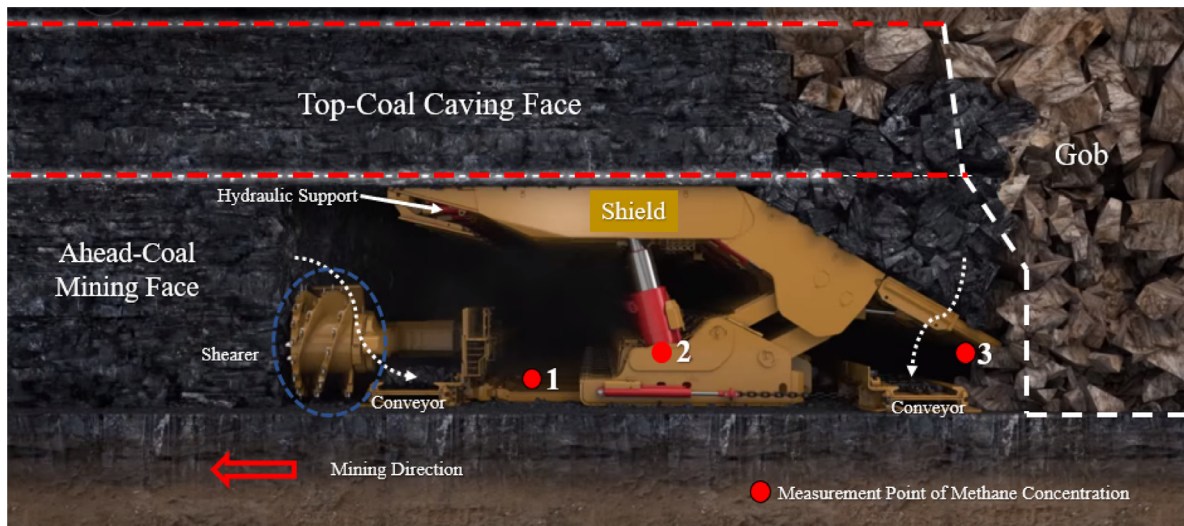
Fig. 1. Schematic of the LTCC mining method (adapted from Caterpillar Global Mining – CAT publication)

concurrent migration of methane. The caved zone (or "gob") may reach ∼4-to-11 times the thickness of the coal seam height where overburden rocks are weak and porous [11,12].

Despite its efficiency and economic favorability, LTCC mining also presents the potential to increase the accumulation of methane at or near the active working face as a consequence of high methane emissions from the gob. The interface between the longwall face and the gob is particularly vulnerable to such accumulations of methane [13–15]. Unfortunately, a series of methane-related incidents have originated from accumulations at or near this interface where accidental ignition has occurred. For example, the occurrences of methane ignitions at the Upper Big Branch South Mine in 1997 and 2010 led to disastrous results, the latter resulting in a massive mine-wide explosion [16].

The provision of an effective ventilation system is necessary to mitigate the gas hazard at the longwall face. A key component is in providing fresh air to miners as well as diluting methane to a safe threshold value below the ignition/explosive limit [17,18]. Previous studies have demonstrated that multiple factors affect the effectiveness of the ventilation system, including the geometry of the ventilation network, airway resistance, airway temperature, operating characteristic of fans together with other features [19–21]. More importantly, excess and unpredicted methane emissions may disturb the ventilation system and present an unexpected hazard to the face with impact on other related ventilation branches [12,22]. LTCC mining is particularly vulnerable in this regard as the methane emissions can be excessive – the method intrinsically creates a huge and irregular caved void behind the shied which is directly connected to the face. Thus, the monitoring and prediction of gas emission patterns and their dilution at face and in the gob region are crucial to allow safe mining. However, it is also technically challenging due to the complexity of the gas emission and transport behavior in the heterogeneous gob materials which provides an uncertain methane source term.

This study documents a mine-wide ventilation pressure and flow rate survey (*p-Q* survey) to establish a ventilation network model – including methane gas concentrations recorded at selected face locations. We develop a numerical gas emission model specifically to dynamically evaluate methane production and transport from the compacted gob and its impact on the longwall face. The numerical model is validated using the mine-wide field methane monitoring results. We use this model to evaluate gas emission intensity from the gob and its interaction with ventilation systems. The validated model is then used as mechanism-based model to investigate the interactions between gob gas emission and the mine ventilation system.

2. Background and literature

Gas emission rate from the gob is closely related to the caving characteristics of the caved rock mass, block size, compaction behavior and evolving porosity and permeability [12,23]. Typically, these characteristics determine the gob gas emission behavior and ultimately influence the ventilation design and effectiveness at the longwall working face [11]. Despite the importance of these characteristics, direct field measurements of porosity and permeability are rare, due to the extremely challenging environment [12]. Thus, many previous studies have attempted theoretical predictions of porosity and permeability which have then been calibrated against field measurements and laboratory data [12,23–26].

Laboratory tests on rock materials, with approximate particle size gradations of the actual gob material from headgate entries in Eastern Kentucky coal mines, have been used to determine the mechanical properties of the gob for numerical models [27]. Such models have been extended to define the porosity and permeability of the broken rock material within the gob [12]. This approach was inspired by the imaging analyses of gob materials to represent the response of a completely fragmented porous medium and constrained relative to observed vertical strains [28]. Some models have used Carman-Kozeny relations to define permeability in the vertical direction [29] with conceptual models of broken rock mass compaction based on the constitutive laws of the broken rock mass [11].

Based on the previous modelling work, a quantitative gas flow model is evidently still lacking – specifically one that can quantify the gas emission rate from the gob towards the face and its adjacent regions including the bleeder system. The pressure gradients driving gas flow in the compacted gob can be directly used to predict gas emission rates under various conditions. The widely used pressure equation for packed beds [30] accommodates both viscous and kinetic energy losses primarily in laminar and turbulent flows, respectively [31–33]. The two principal constants in Ergun's equation were actively discussed and subsequently modified by Hicks (1970) by replacing the two constants with the Reynolds number [34]. Potentially difficult to apply to heterogenous irregularly packed beds accommodations for the impacts of contracting-
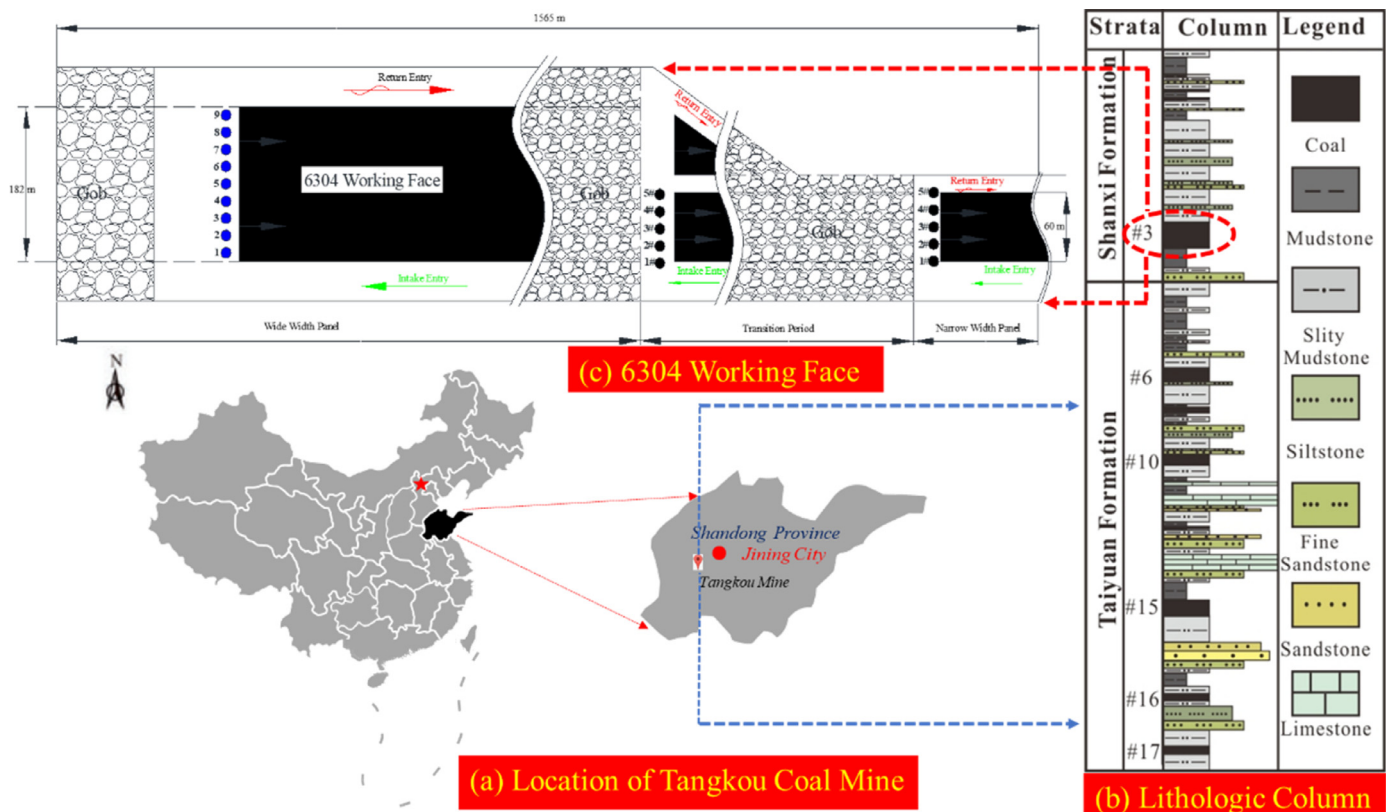
Fig. 2. Location and schematic of the Tangkou coal mine and the 6304 working face. (a) Location of Tangkou coal mine. (b) Lithologic column. (c) 6304 working face.

expanding channels [35] have ameliorated these difficulties, including the accommodation of viscous and kinetic energy losses [36].

To summarize, the aforementioned studies established a spectrum of models and methods to accommodate flow and transport in packed beds. However, compacting coal mine gobs are a particularly unique packed bed undergoing dynamic compaction and with an unusually irregular size and shape distribution of rock-coal blocks. Needed is a mechanism-based flow model with physically meaningful parameters that may be validated to predict gas emissions from gob. We introduce and validate a gas flow behavior is modelled and gob gas emission rate is defined and quantified by numerical simulation. This coupled analytical and numerical modeling framework provides a pathway to quantify the gas emission rate from the compacted gob within the mine while correctly considering the detailed component material properties of the gob.

3. Mine site description for the field monitoring

We conducted a mine-wide field monitoring program in a deep longwall mining operation. The Tangkou coal mine is located in Jining city, Shandong Province, China (Fig. 2(a)). The coal seams are Permian (Shanxi formation) and Carboniferous (Taiyuan formation) (Fig. 2(b)) comprising six mineable seams – these are seams #3, #6, #10, #15, #16 and #17 as shown in Fig. 2(b). Among these six minable coal seams, #3, #16 and #17 are the primary targeted seams for current mining with annual production planned at ∼5 million tons/yr.

The principal coal block is largely free from large scale faulting. The #3 coal seam is being mined by the LTTC mining method. Our field survey was conducted at the 6304 working face of the #3 coal seam with the panel layout shown in Fig. 2(c). The average thickness of the coal seam at the 6304 working face is ∼ 9.76 m and in-

clined at between 0∼10° (average angle is ∼ 4°) to the horizontal. The panel is constrained by geological to be of variable width. An initial width of 182 m transitions to a final narrow panel width of 60 m with a working face length of ∼1565 m. The virgin methane gas content and pressure are measured at 4.8 m³/t and 0.72 MPa, respectively. The comprehensive mine ventilation survey and the gas concentration inventory at designated locations constrains the model development noted later in this work.

4. Analytical and numerical models for determining gas flow

Compacting coal mine gobs are a unique form of packed bed undergoing dynamic compaction and with an unusually irregular size and shape distribution of rock-coal blocks. The rock-coal blocks in the caved zone create viable pathways for airflow and the concurrent migration of methane. We develop a physics-based model to accommodate gas desorption from the blocks and then transport within the voids that accommodates both viscous and inertial losses.

4.1. Conceptual physical model

In LTCC mining operations, the caved gob zone is continuously filled with the residual coal and rock blocks breaking from the roof. The gob, therefore, can be classified as a unique porous medium consisting of roof rock blocks and residual coal associated with voids. The tortuous flow channels within the voids provide channels for gas and fluid migration. The architecture and composition of the rock and coal block mixture determines the critical features of the gob, including porosity, permeability, connectivity and compactive behaviors, among others. Despite the complex characteristics of the compacted gob, a conceptual physical model
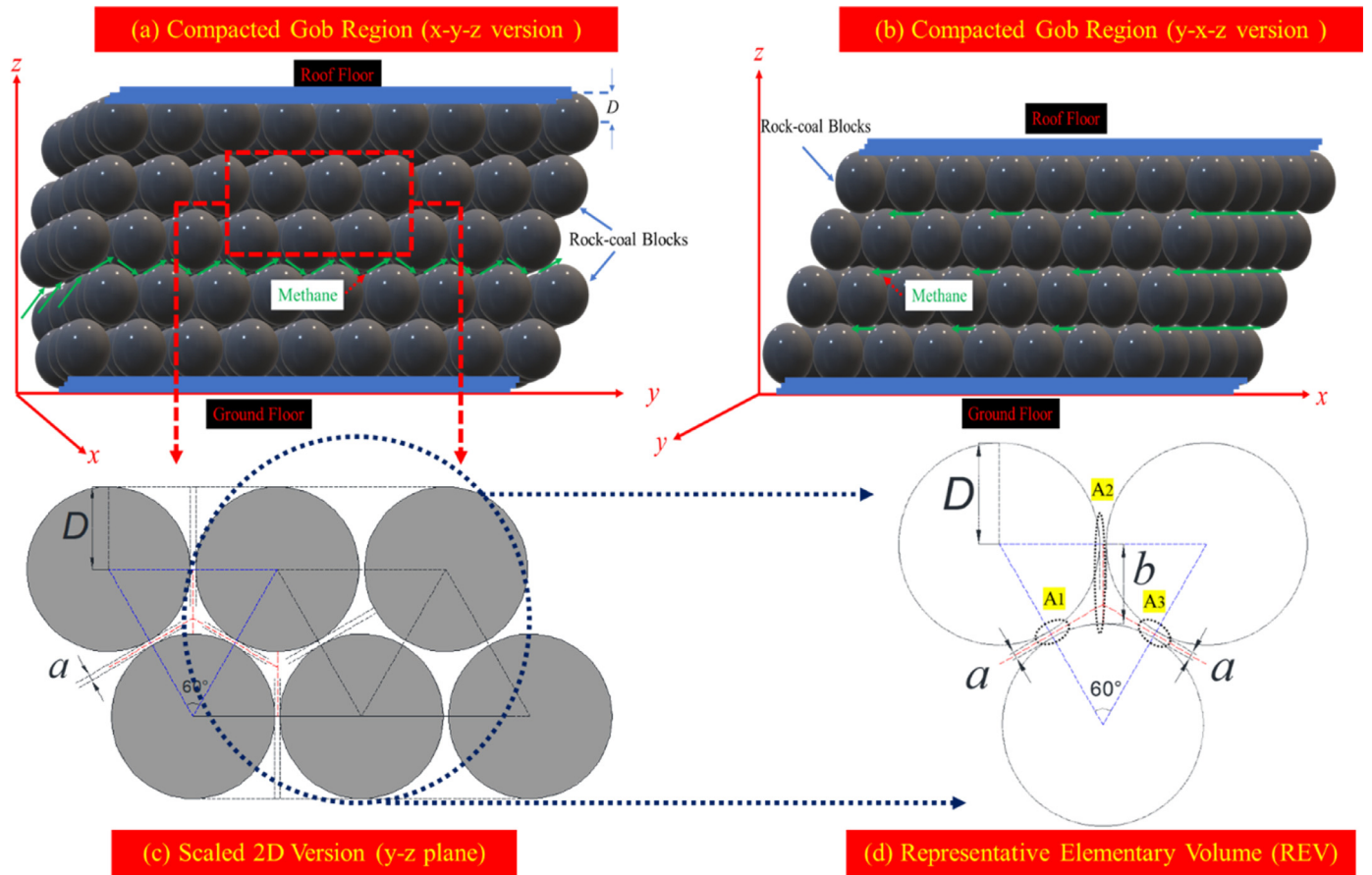
Fig. 3. Schematic of the distribution of rock-coal blocks in the gob. (a) 3D version (*x-y-z*) of the compacted gob region, with *x, y* and *z* directions representing horizontal direction along the gob width, horizontal direction along with gob length and vertical direction along with gob height respectively. (b) 3D version (*y-x-z*) of compacted gob region. (c) Scaled 2D version in the *y-z* plane. (d) Representative elementary volume (REV)

must incorporate the key physical features of the assemblage – selected in 3D and 2D in Fig. 3. We assume a layered assemblage of spherical blocks (Fig. 3 (a)), with each layer of the spheres in the *x-y* plane distributed center-to-center. Caved voids exist between spheres and are evenly spaced. Fig. 3 (b) shows the distribution of spheres in the *y-x-z* version. Similarly, each layer of the spheres in the *y-x* plane are distributed by point contact and different layers in *z* direction are interrelated. If the pressure gradient is defined from the pressure difference between the deep gob and the working face, the gas flow direction is as represented by the green arrows in Fig. 3(a) and (b). From Fig. 3(c) and (d), it is apparent that methane will pass through the irregular void channels. The radius of the spheres is represented as D with the void channel widths defined as a or b in Fig. 3(c). The irregular void channels also result in variable cross-sectional areas such as A1, A2 and A3 in the 3D version (A1 is equivalent to A3 in this conceptual physical model). Gas migrates in the direction of the pressure gradient with total energy losses comprising the sum of viscous losses and kinetic losses resulting from spatial accelerations due to changes in cross-sectional areas [37]. Other key assumptions behind the model are: (1) the dynamic process of mechanical compaction in the gob is not accommodated, that is, the caved gob region exists in its final compacted state; (2) the mixture of rock blocks and residual coal are regarded considered as an isotropic and homogeneous porous medium – although this assumption may be relaxed; (3) methane content in the gob consists of free gas in the developed voids and adsorbed gas in the rock-coal blocks; (4) gas ad/desorption processes are isothermal; (5) effects of the deep gob region (depth

over 50 m) and adjacent coal seams on gob gas emissions are neglected.

4.2. Pressure gradient within the packed-bed gob

The pressure gradient in this porous packed medium can be given by the Poiseuille equation [30]:

$$\frac{dp}{dL} = \frac{32\mu\tau V_\infty}{d^2} \tag{1}$$

where, $\frac{dp}{dL}$ is the pressure gradient induced by viscous flow (Pa/m); p is the pressure (Pa); *L* is the length along the direction of the pressure gradient (m); *d* is the capillary diameter (m); μ is the dynamic viscosity (Pa·s); τ is the tortuosity (dimensionless); V_∞ is the absolute fluid velocity in the cross-section of the capillary (m/s), which scales with the apparent velocity at the cross-section of the whole cross-section, $V_\infty = \frac{V_a}{\phi}$ [38] and where ϕ is porosity (dimensionless). Therefore, Eq. (1) can be re-arranged as:

$$\frac{dp}{dL} = \frac{32\mu\tau V_a}{\phi d^2} \tag{2}$$

In Eq. (2), the capillary diameter *d* can be represented by hydraulic diameter d_h (m) [39]. d_h can be defined as:

$$d_h = 4\frac{A}{C} \tag{3}$$

where, *A* is the cross-sectional area of the fluid flow (m²); *C* is the wetted perimeter of the cross-section (m). Moreover, Eq. (3) can be

further expressed as:

$$d_h = 4\frac{A\tau L}{C\tau L} = 4\frac{A\tau L}{V_p}\frac{V_p}{C\tau L} = 4\frac{\phi}{S_v} \tag{4}$$

where, V_p is the volume of the porous medium (m^3); ϕ is the porosity (dimensionless) and S_v is the specific surface area (m^{-1}), where the specific surface area is defined as the total surface area of the porous medium per unit bulk volume.

For the gob packing materials, according to the conceptual geometry of Fig. 3(a) and (b), the surface area of the transporting capillaries can be estimated as:

$$S_v = \frac{n4\pi D^2(1-\phi)}{n\frac{4}{3}\pi D^3} = \frac{3(1-\phi)}{D} \tag{5}$$

where, n is the numbers of rock-coal blocks (dimensionless) and D is the uniform radius of the rock-coal blocks (m).

By substituting Eqs. (4) and (5) into Eq. (2), the pressure gradient due to the viscous energy loss becomes:

$$\frac{dp}{dL} = \frac{18\mu\tau V_a(1-\phi)^2}{\phi^3 D^2} \tag{6}$$

As illustrated in Fig. 3, the cross-sections of gas flow channels are irregular and thereby kinetic energy loss should be taken into consideration. For uniform capillaries, the kinetic energy loss is a function of velocity with a quadratic dependancy, which can be expressed as [30]:

$$\frac{dp}{dL} = \frac{1}{2}\frac{\rho V_\infty^2}{d} \tag{7}$$

where, ρ is fluid density (kg/m^3). However, the capillaries in the geometric model are irregular. Correspondingly, Zhang et al. (1999) and Wu et al., (2008) modified the kinetic energy equation as [36,40]:

$$\frac{dp}{dL} = \frac{1}{2}\xi\frac{\tau\rho V_\infty^2}{d} \tag{8}$$

where, ξ is a coefficient which may be estimated from changes in different cross-sectional areas.

From cross-sectional area A_1 to A_2, as shown in Fig. 3(d), the area gradually expands. Here the cross-sectional areas A_1 and A_2 are the products of the void widths and void extension length in the negative x-direction. The corresponding coefficient induced by an increment of cross-sectional area can be expressed as [36,40]:

$$\xi_1 = \left(1 - \frac{A_1}{A_2}\right)^2 \tag{9}$$

From cross-sectional area A_2 to A_3, as shown in Fig. 3(d), the cross-sectional area gradually decreases. The definitions of cross-sectional areas A_2 and A_3 are the same as previous. The corresponding coefficient induced by the cross-sectional area decreasing can be expressed as [36,40]:

$$\xi_2 = 0.5\left(1 - \frac{A_3}{A_2}\right) \tag{10}$$

Based on the representative elementary volume (REV) - the dashed equilateral triangle in Fig. 3(d) - the relationship between the size of the rock-coal block and porosity can be expressed as:

$$(1-\phi)A_{REV} = \frac{1}{2}\pi D^2 \tag{11}$$

where, A_{REV} is the cross-sectional area (m^2) of the REV. This may also be represented by $A_{REV} = \frac{\sqrt{3}}{4}(a+2D)^2$ based on geometric relationships, where a is the void width (m), where inserting into Eq. (11) yields:

$$\alpha = \frac{a}{D} = 3^{-\frac{1}{4}}\sqrt{\frac{2\pi}{1-\phi}} - 2 \tag{12}$$

where, α is the ratio of void width to the radius of the rock-coal block (dimensionless).

In terms of the geometric relationship in Fig. 3, the diameter of the cross-section A_2 can be expressed as:

$$b = \frac{\sqrt{3}}{2}a + (\sqrt{3}-1)D \tag{13}$$

Substituting Eq. (12) into Eqs. (9) and (10) yields:

$$\xi_1 = \left(1 - \frac{a}{b}\right)^2 = \left(1 - \frac{1}{\frac{\sqrt{3}}{2} + (\sqrt{3}-1)\frac{1}{\alpha}}\right)^2 \tag{14}$$

$$\xi_2 = 0.5\left(1 - \frac{a}{b}\right) = 0.5\left(1 - \frac{1}{\frac{\sqrt{3}}{2} + (\sqrt{3}-1)\frac{1}{\alpha}}\right) \tag{15}$$

Substituting Eqs. (14) and (15) into Eq. (8) yields:

$$\frac{dp}{dL} = \frac{1}{2}(\xi_2 + 4\xi_2^2)\frac{\tau\rho V_\infty^2}{d} = \frac{3}{8}(\xi_2 + 4\xi_2^2)\frac{\tau\rho V_a^2(1-\phi)}{\phi^3 D} \tag{16}$$

Gas flow is driven by pressure gradient with the combined impact of viscous and kinetic energy losses contributing to this pressure loss. The pressure gradient may therefore be obtained by combing Eqs. (6) and (16) as:

$$\nabla p = \frac{18\mu\tau V_a(1-\phi)^2}{\phi^3 D^2} + \frac{3}{8}(\xi_2 + 4\xi_2^2)\frac{\tau\rho V_a^2(1-\phi)}{\phi^3 D} \tag{17}$$

In Eq. (17), the first term on the right represents the viscous energy loss as a linear function of apparent velocity, with the second term representing kinetic loss as quadratic function of apparent velocity.

4.3. Governing gas flow equation in a packed-bed

The mass conservation equation for each gas component is given as:

$$\frac{\partial m}{\partial t} + \nabla\left(\rho_g\vec{V_a}\right) = q_s \tag{18}$$

where, ρ_g is the methane density (kg/m^3); $\vec{V_a}$ is the non-Darcian velocity vector (m/s); t is real time (d); q_s is the normalized gas source rate (kg/(kg·s)); m is the gas content (kg/m^3), comprising states of free-phase gas and adsorbed gas [41,42]. The gas content is defined as:

$$m = \rho_g\phi + (1-\phi)\rho_{ga}\rho_c V_g \tag{19}$$

where, ρ_{ga} is the gas density under standard conditions (kg/m^3); ρ_c is the coal density (kg/m^3); V_g is the average remaining gas content in the granular matrix at an equilibrium state (V_{gd}) with the gas pressure p recovered from the Langmuir equation [43]:

$$V_{gd} = \frac{V_L p}{p + p_L} \tag{20}$$

The methane density may be represented by the ideal gas law as:

$$\rho_g = \frac{pM}{RT} \tag{21}$$

where, M is the molecular weight of methane (kg/mol); R is the universal gas content (J/(mol·K)); and T is temperature (K).

Eq. (17) gives the pressure gradient, which describes the viscous energy loss and kinetic energy loss in the non-Darcy flow within the gob. From Eq. (17), the equivalent non-Darcyian velocity vector of fluid flow is derived as:

$$\vec{V_a} = -\left[\frac{18\mu\tau(1-\phi)^2}{\phi^3 D^2} + \frac{3}{8}(\xi_2 + 4\xi_2^2)\frac{\tau\rho V_a(1-\phi)}{\phi^3 D}\right]^{-1}\nabla p \tag{22}$$

Reynolds number (R_e) is a dimensionless number relating the ratio of viscous to inertial (kinetic) losses [30], which is defined as:

$$R_e = \frac{\rho D V_a}{\mu} \qquad (23)$$

Eq. (22) can be transformed using the Reynolds number as:

$$\vec{V_a} = -\left[\frac{18\mu\tau(1-\phi)^2}{\phi^3 D^2} + \frac{3}{8}\left(\xi_2 + 4\xi_2^2\right)\frac{\tau\mu(1-\phi)}{\phi^3 D^2} R_e \right]^{-1} \nabla p \qquad (24)$$

Substituting Eqs. (19)-(21) and (24) into Eq. (18), the governing equation for gas flow in the gob can be defined as

$$\left(\frac{M\phi}{RT}\right)\frac{\partial p}{\partial t} - \nabla \left\{ \frac{pM}{RT}\left[\frac{18\mu\tau(1-\phi)^2}{\phi^3 D^2} + \frac{3}{8}\left(\xi_2 + 4\xi_2^2\right)\frac{\tau\mu(1-\phi)}{\phi^3 D^2} R_e \right]^{-1} \nabla p \right\} = -(1-\phi)\rho_{ga}\rho_c\frac{\partial V_g}{\partial t} + q_s \qquad (25)$$

The remaining gas content in the granular matrix can be calculated from the quasi steady-state equation for methane desorption [44,45], given by

$$\frac{\partial V_g}{\partial t} = -\frac{1}{t'}\left(V_g - V_{gd}\right) \qquad (26)$$

where, t' is the gas diffusion time (s).

Eqs. (25) and (26) represent the governing equations of gas flow. Specifically, Eq. (25) defines the methane flow equation, where methane content consists of both free-phase gas and adsorbed gas components. Eq. (26) defines the methane desorption process, which will contribute the total methane flow and determine the apparent gas flow rate from the gob. The broken rock blocks in the caved zone is gradually compacted under the near constant overburden loading stress for underground longwall coal mining. The loading stress over the gob evolves with time and the gob compaction process on caved coal measure rocks can be described as a one-dimensional quasi-static consolidation. Thus, the effects of the dynamic gob compaction behaviors on fugitive gas emission process should be involved into the proposed model. As quantified by Eq. (25), two main parameters including the uniform radius of the rock-coal blocks (D) and the gob porosity (ϕ) can be used to quantify the effects of the dynamic gob compaction behaviors on fugitive gas emission process, as discussed in Section 6.1.

5. Results and analyses

Field measurements of airflow quantities and methane concentrations were conducted at the 6304 working face of the Tangkou coal mine. The measured methane concentrations and airflow quantities were used to estimate the average gas emission rates from the compacted mine gob and to validate numerical implementations of the gob emission model described in the previous. These results can ultimately provide the data for analyzing the interactions between the caved gob and the ventilation system and to define mitigation strategies to minimize gas concentrations and hazard.

5.1. Field work results

As discussed in Section 3, there are three discrete geometries of the panel, defined by width. For the *in situ* methane concentration monitoring, nine evenly spaced field measuring stations (L1, L2, L3...L9) were located at the active working face for the widest panel. Five evenly spaced measuring stations were located in the transition and narrow panels, respectively, as illustrated in Fig. 4(b). At each gas concentration measuring station, three measuring points (M1, M2, M3) were designated, as shown in Fig. 4(a).

Average gas concentrations were determined from the mean of the group of three monitoring points at each station with each group measured three times and again averaged. Fig. 4(c) shows field measurements being taken at the three corresponding measurement points at a given measuring station with these data listed in Table 1.

Based on the field investigation data in Fig. 5 and Table 1, we can estimate the gas emission rates from the gob by using the methane concentration at the working face in conjunction with air quantities in the intake and return airways. From Fig. 5, the average methane concentration at the active portion of the wide panel is higher than that of transition panel. Also, the methane concentrations at the narrow panel are clearly lower than those of the two previous panels, which can be attributed to the lower production capacity at the narrow panel. For each of the measuring station, the difference between three measurement points are insignificant, suggesting that the average methane concentration should be sufficient for modeling. This observation of homogenized methane concentrations suggests turbulent mixing at the face - desirable to prevent methane layering and concentration.

Methane concentration monotonically increases from headgate to tailgate (Fig. 5). This finding is also expected, as the methane incrementally accumulates from discharges along the longwall panel face, from headgate to tailgate. Empirical regression of the average methane concentration with distance from the headgate show a strong linear correlation as shown in Fig. 6. We used the fitted linear relationship to estimate the average methane concentration for the working panel at different stages of development, including for the wide (182 m), transition (141 m) and narrow (60 m) panels. For example, the fitted linear relationship between the average methane concentration at a given location and the distance from the intake entry during the excavation of the wide panel is shown as $y = 0.00367x + 0.1601$ (Black line in Fig. 6). The average methane concentration over the entire panel is defined as $\bar{C}_1$ and calculated from $\frac{\int_0^{182}(0.00367x+0.1601)dx}{182}$, is ~ 0.494. Methane concentrations are similarly estimated during the successive recovery of the different panels with these data listed in Table 2. Then, we assume the relation between air quantities in the intake and return airways can be expressed as:

$$Q_r = Q_e + Q_i \qquad (27)$$

where, Q_i and Q_r are air quantities in intake and return airways (m³/s); Q_e is the gas emission quantity (m³/s), which mainly consists of air-methane emission quantity from gob, methane emission quantity from panel and possible air leakage quantity from adjacent strata. It is apparent that the gas emission rates from gob to face can be quantified as,

$$q_e = Q_e\bar{C}_i \qquad (28)$$

where $\bar{C}_i(i=1, 2, 3, \cdots)$ is the average methane concentrations distributed along with the working face (%); and q_e is gas emission rate (m³/s).

Gas emissions (Q_e) could emanate from several sources including air-methane emissions from the gob, methane emissions from the panel and possible air leakage from adjacent strata, but it is difficult to distinguish and accurately estimate the amount coming from each source. For this particular mine, there is no bleeder system and the burial depth of the coal seam is deep ($\sim$950 m), therefore it is reasonable to assume the gas emission is only from gob and for pure methane. To calculate the reliable and real-time

(a) Three Measurement Points at Each Location

(b) Measurement Locations: L1, L2, L3…

(c) Field Measurement Point M1

(d) Field Measurement Point M2

(e) Field Measurement Point M3

Fig. 4. Field investigation locations and measurement points at 6304 the longwall working face. (a) Three measurement points, M1, M2 and M3, are defined at each location. (b) Distributions of investigation locations at the 6304 working face. (c), (d), (e) Field investigator sampling.

Table 1
Field investigation recovered methane concentrations (%) in the three panel geometries.

	Field investigation date and measurement points (M1, M2 and M3)												
	06/09/2018			08/04/2018				11/10/2018			11/12/2018		
	Wide panel			Transition panel				Narrow panel					
	M1	M2	M3	M1	M2	M3		M1	M2	M3	M1	M2	M3
L1	0.24	0.24	0.25	0.18	0.18	0.18	L1	0.11	0.11	0.11	0.12	0.11	0.13
L2	0.26	0.26	0.28	0.22	0.22	0.20	L2	0.18	0.18	0.19	0.19	0.19	0.21
L3	0.26	0.26	0.28	0.31	0.30	0.32	L3	0.25	0.24	0.26	0.26	0.26	0.28
L4	0.32	0.32	0.34	0.32	0.32	0.34	L4	0.29	0.28	0.29	0.30	0.29	0.31
L5	0.49	0.48	0.49	0.36	0.36	0.36	L5	0.36	0.34	0.36	0.35	0.34	0.37
L6	0.53	0.53	0.55	0.38	0.36	0.40							
L7	0.71	0.70	0.72	0.40	0.40	0.46							
L8	0.75	0.75	0.76	0.43	0.42	0.40							
L9	0.85	0.85	0.87	0.62	0.60	0.64							

Table 2
Gas emission rates.

Parameters	Location	June 9th, 2018	Aug 4th, 2018	Nov 10th, 2018	Nov 12th,2018	Source
Air Quantity(m^3/s)	Intake Entry	40.60	40.10	22.50	22.09	Field Monitoring
	Return Entry	41.83	41.33	23.40	22.99	Field Monitoring
Average Methane Concentration (%)	Working Face	0.494	0.355	0.247	0.237	Integration
Average gas emission rate (m^3/s)	Gob	0.0061*	0.0044*	0.0022*	0.0021*	Estimated

* The actual gas emission rate is lower than this maximum theoretical value.
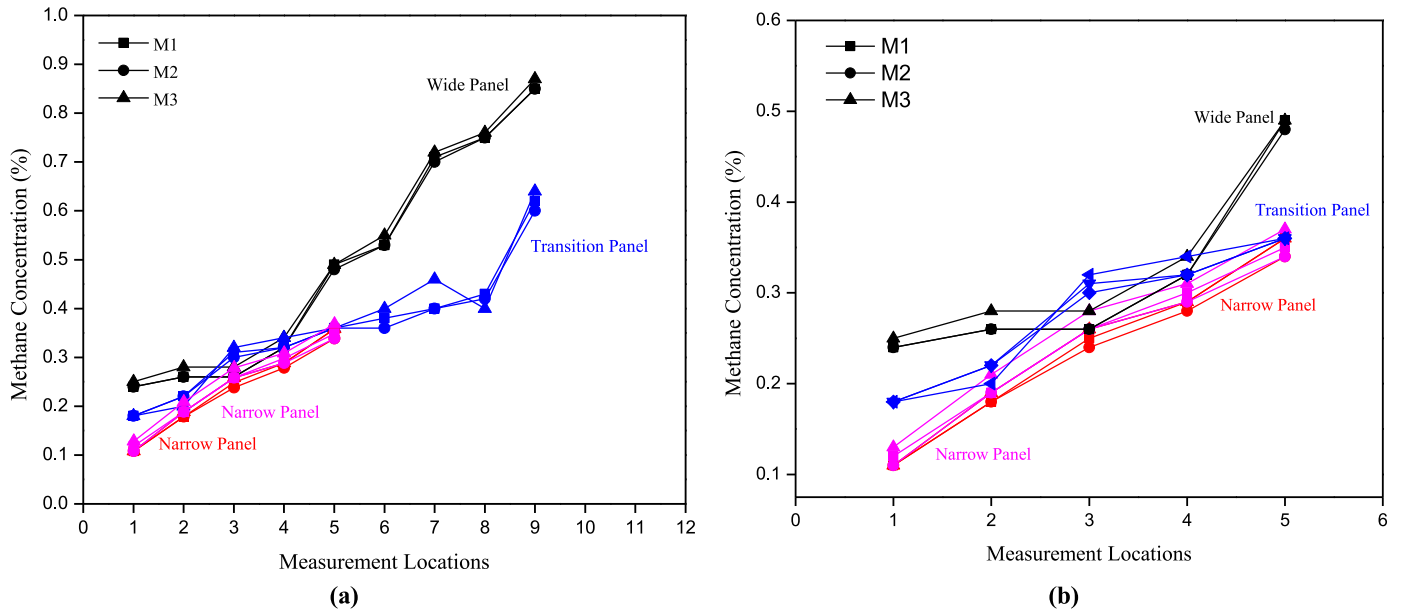
Fig. 5. Field methane concentrations at investigation locations. (a) Nine locations at the widest portion of the panel (June 9th, 2018), transitional section (Aug 4th, 2018) and narrow panel section (Nov 10th and 12th, 2018). (b) Normalized methane concentrations at the same five locations.
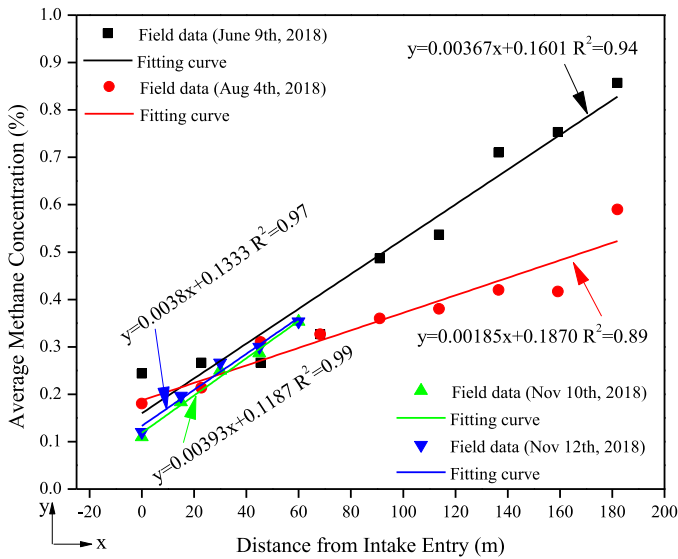

Fig. 6. Distributions of average methane concentrations at the 6340 working face.

methane concentration, the stable mine ventilation status during the operation of 6304 working face was initially assumed. To justify this assumption, we conducted the mine-wide ventilation during the mining operation period of 6304 working face (June 9th, 2018), the ventilation survey result was shown in Fig. 13. From the ventilation survey results, the air quantity at 6304 working face during the wide panel period is ~40.6 m³/s. Then we monitored the methane concentration at different times (June 9th, 2018; Aug 4th, 2018; Nov 10th, 2018; Nov 12th, 2018), and we simultaneously recorded the airflow quantity when we tried to monitor the methane concentration (as illustrated in Table 2). The results in Table 2 shown that the air quantities at June 9th, 2018 and Aug 4th, 2018 were almost same, which were 40.6 m³/s and 40.10 m³/s respectively. Similarity, the air quantities at Nov 10th, 2018 and Nov 12th, 2018 (the time during the narrow panel period) were also almost same, which were 22.50 m³/s and 22.09 m³/s respec-

tively. The field gas emission rates were estimated and all the results are listed in Table 2.

5.2. Numerical modeling of gas flow

COMSOL Multiphysics was employed to simulate gas flow in the compacted gob and to predict the gas emission rates. In order to validate the numerical simulation model, methane concentrations measured at the 6304 working face were used, as presented in Section 5.1. Accurate estimation of the gas emission rates from the gob at any given time is challenging due to the complex mining environment and working conditions. Based on the mine field visit and the layout of 6304 working face (Fig. 2(c)) developed from real mine map, the regular layout of 6304 working face can help simplify the spatial layout 6304 working face from 3D version to 2D version, and thus the cutaway of the 6304 working face (Fig. 4(b)) can be established as the geometry model.

The caving ratio, rear support length and rear support angle define the geometric arrangement at the face, as shown in Fig. 7. The caving ratio represents the ratio of caving thickness to the excavated height, as shown in Fig. 7(d). The rear support length and rear support angle are the horizontal control length of the rear support of the shield and the angle between rear support shield and level ground, as illustrated in Fig. 7(d). The caving ratio is ~1.4 for the 6304 working face. The rear support length is a fixed value at 1 m behind the rear support shield (Fig. 7(c)) and the rear support angle is 45°. A schematic of the face is illustrated in Fig. 7(c). Fig. 7 (b) shows a caving thickness of ~5.6 m and therefore the excavated height is ~ 4 m (average thickness of the coal seam is ~ 9.6 m). The top caving zone is represented in the vertical direction by boundary ① in Fig. 7 (b), which is separated from the excavated panel by the top shields. Boundary ① is termed the caved-zone line. Boundaries ② and ③ represent the tilted shield and top-coal caving gate as shown in Fig. 7 (b). Thus, it is clear that boundary ③ will be the gas emission boundary between the 6304 working face and the gob. Boundaries ④, ⑤ and ⑥ represent the ground floor, rear boundary and immediate roof as shown in Fig. 7 (b). Whittaker and Singh (1979) assumed that the gob can recover its original stress at a distance of ~45 m from the face. Using Flac³D, Abbasi et al. [50] estimated the mechanical response
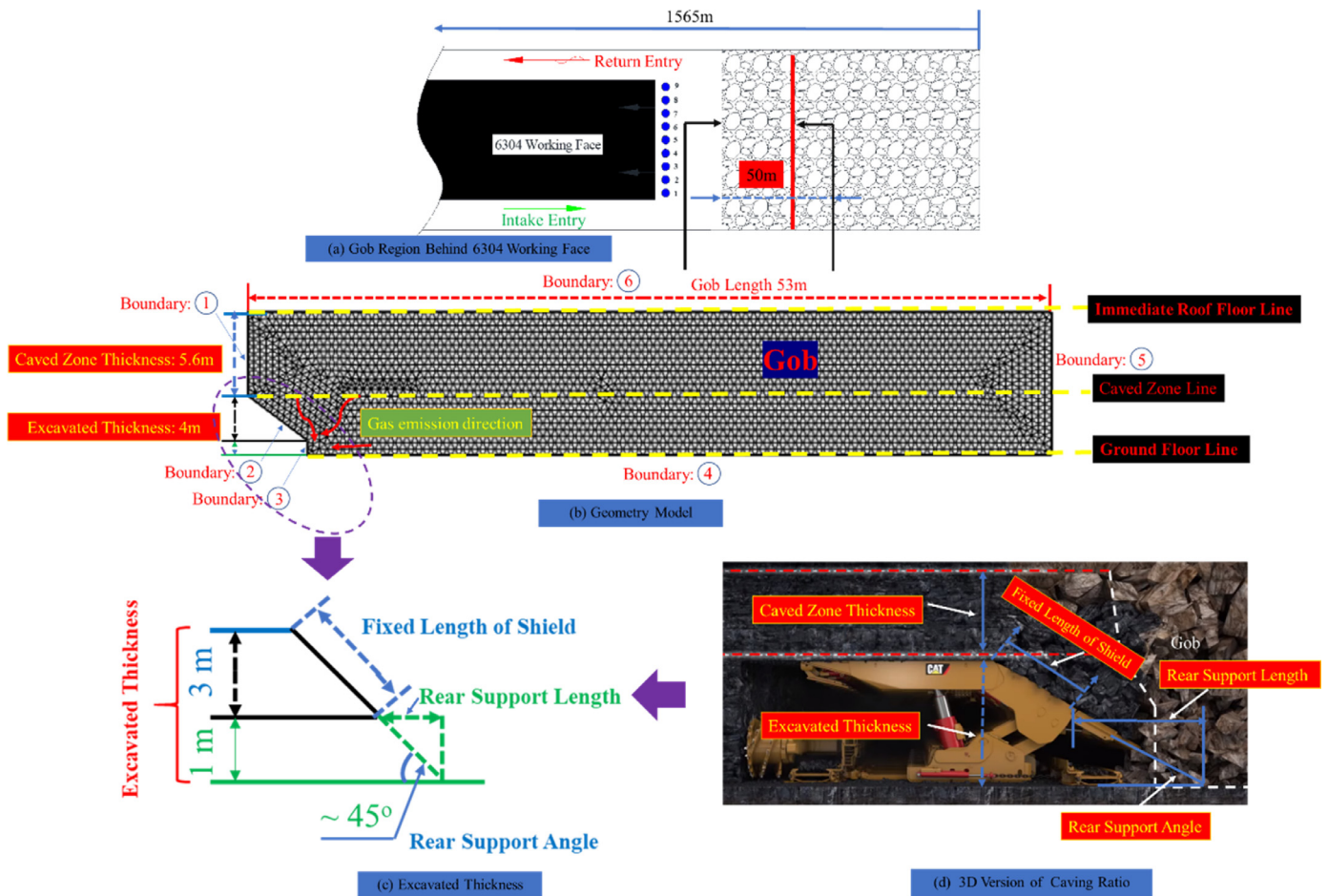
Fig. 7. Geometric model for compacted gob and boundary locations. (a) Top view of gob region behind the 6304 working face. (b) Cutaway vies of geometric model. (c) Geometry of the excavation. (d) 3D View of the excavation.

of the gob from field measurements. The results indicate that the gob achieves pre-mining overburden stress at ∼55 m behind the back-end of the shields. If we assume that the gas stored in the compacted gob region recovered to pre-mining overburden stress has negligible influences on the face, it is reasonable to preset the gob length as ∼50 m in our model, as illustrated as the length of boundary ④. In LTCC mining, the caving region over the shield will also affect gas emission rates at boundary ③. Summing gob length and shield supported distances yields a total length of boundary ⑥ as 53 m.

Input parameters are key in determining the fidelity of the final results. Unfortunately, only sparing data are available. Laboratory tests on rock materials, with approximate particle size gradations of the actual gob material recovered from headgate entries in Eastern Kentucky coal mines, have been used to determine the mechanical properties of the gob for numerical models [27]. A set of physically meaningful data based on physically similar laboratory samples have been obtained [27]. The experimental data have been screened against predictive porosity and permeability models [12]. Thus, some parameters were taken from the literature. The mine specific data were either measured in the laboratory or recovered from the field. The Reynolds number can be determined by field survey of velocity and other known parameters of gas density, gas dynamic viscosity and an assigned characteristic dimension. Another parameter is the methane diffusion time in the homogenous rock-coal porous medium constrained by the diffusion coefficient of pure methane in the coal matrix. All parameters are as listed in Table 3.

Moreover, the initial and boundary conditions are required for the numerical modeling. In all three cases, the initial conditions with initial gas pressure and content of 0.72 MPa and 2.58 m^3/t respectively are identical. However, different boundary conditions were used. In Case 1, except for the gas emission boundary ③, all the other boundaries were set with zero flux. In Case 2, boundary ① representing the interface between the top-caving region and the gob (Fig. 7(b)) was set as gas source term. In Case 3, gas sources were supplied from boundaries ① and ⑥. The detailed boundary conditions are listed in Table 4.

5.3. Pressure distribution in the caved gob

In order to evaluate gas pressure distribution within the gob, ten monitoring points were set within the simulation model, as shown in Fig. 8. Fig. 9 depicts the distributions of gas pressure
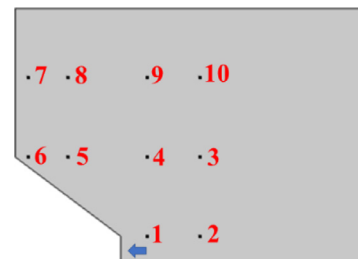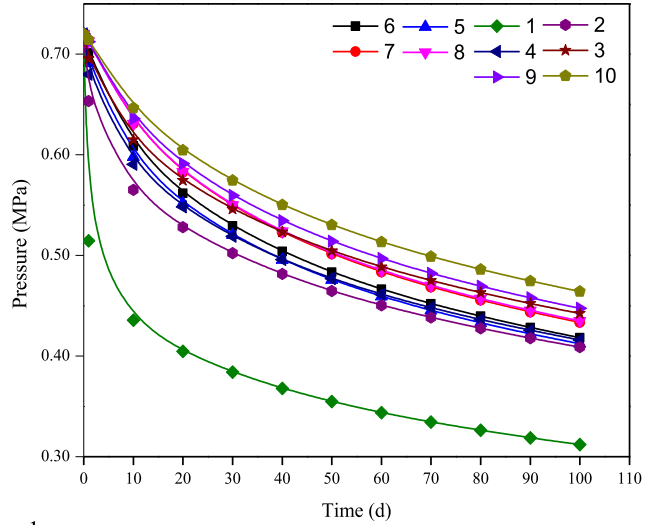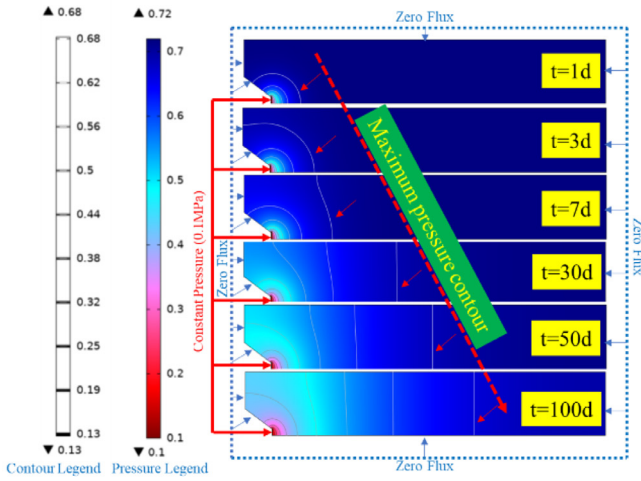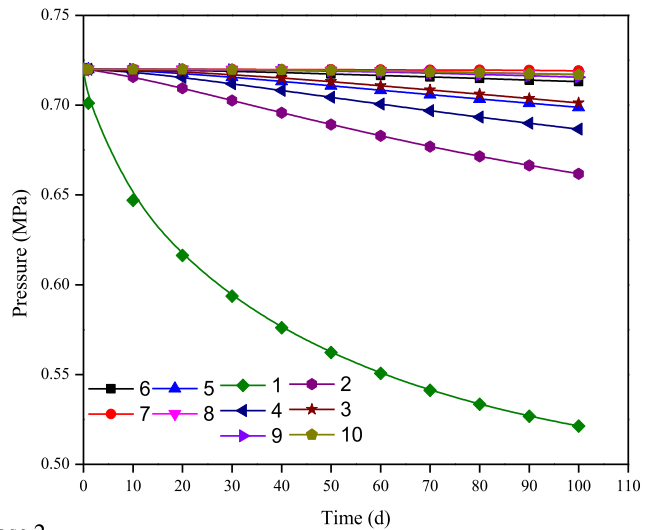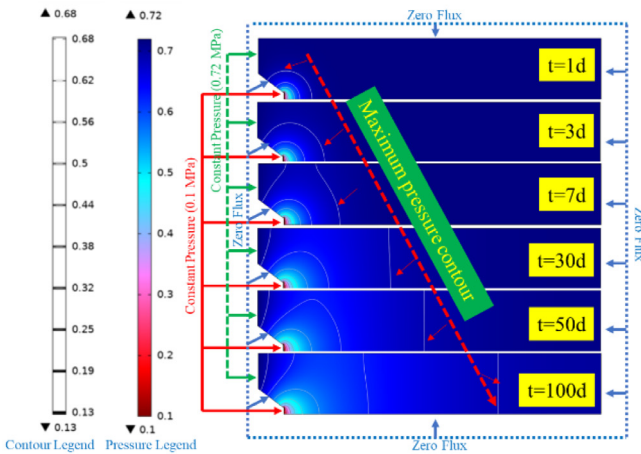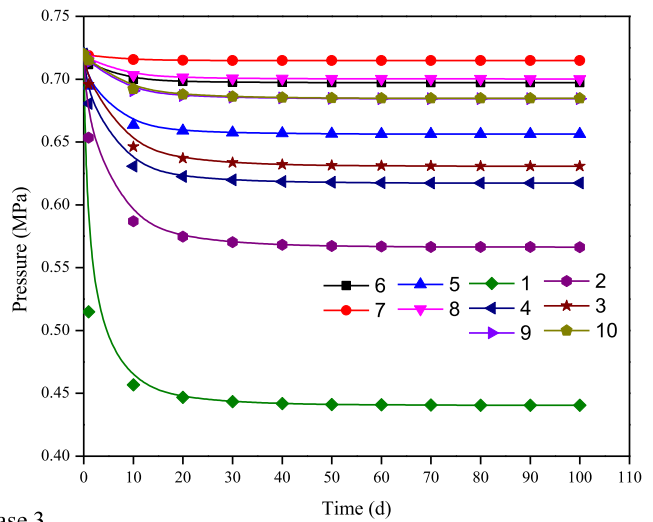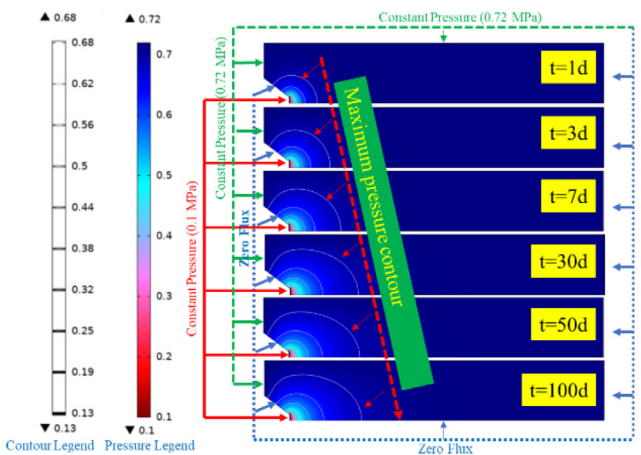

Fig. 8. Distributions of monitoring points.

(a) Case 1

(b) Case 2

(c) Case 3

Fig. 9. Pressure distributions in the gob under different boundary conditions.

Table 3
Basic input parameters.

Parameters	Values	Source
Molar mass of gas (kg/mol)	16.0	Constant
Universal gas constant (J/(mol·K))	8.314	Constant
Temperature (K)	301.0	Field test
Dynamic viscosity (Pa·s)	1.84e−5	Constant
Tortuosity	1.26	Pappas and Mark [27]
Porosity	0.3	Pappas and Mark [27]
Langmuir pressure (MPa)	0.62	Experimental test
Langmuir volume (m^3/t)	4.8	Experimental test
Reynolds number	2.0	Assumed
Block size (cm)	51.0	Pappas and Mark [27]
Rock-coal density (g/m^3)	2.0	Experimental test
Gas density at standard condition (kg/m^3)	0.707	Constant
Initial pressure (MPa)	0.72	Field test
Diffusion time (d)	5.0	Assumed

Table 4
Boundary conditions for three cases.

Cases	Boundaries			
	1	3	6	2&4&5
1	zero flux	$p_{c1}; V_{gc1}$	zero flux	zero flux
2	$p_{c2}; V_{gc2}$	$p_{c1}; V_{gc1}$	zero flux	zero flux
3	$p_{c2}; V_{gc2}$	$p_{c1}; V_{gc1}$	$p_{c2}; V_{gc2}$	zero flux

where, $p_{c1} = 0.1$ MPa; $p_{c2} = 0.72$ MPa; $V_{gc1} = V_L p_{c1}/(p_{c1} + p_L)$; $V_{gc2} = V_L p_{c2}/(p_{c2} + p_L)$.

within the gob under different boundary conditions. In all three cases, gas flow profiles were simulated for one hundred days. In all simulations, we observed that the pressure gradually increases from the rear support gate towards the deep compacted gob with results illustrated by the pressure contours as well as the pressure decline curves as shown in Fig. 9. The rear support gate retains the lowest pressure and the pressure progressively increase towards the gob. As time elapses, the low pressure region move progressively deeper into the gob.

The different boundary conditions noted previously can significantly influence the dynamic pressure profile within the gob. In case 1, zero flux boundary conditions were set on all the boundaries except for the gas emission from the gob boundary ③. Therefore, Case 1 represents the case where gas emission is solely from the caved rock-coal mass. The gas pressure would decrease to zero at very long times (infinite time). In Case 2, there is an additional gas source from boundary ① due to the gas influx from the top-caving region. Thus, gas content supplemented by boundary ① and the initial gas content in the caved gob will induce continuous gas emission from the gob. Compared with Case 1, the pressure depletion is delayed in the gob due to the additional gas source from the top-caved zone. This is illustrated in Fig. 9 where the maximum pressure contour moves towards the face. This is partially apparent from the maximum pressure distribution on the adjacent region at the top-left side, as shown in the pressure decline curve for Case 3 (Points 6 and 7).

The gas emission rate from the gob to the face can be quantified by integrating the velocity function across the gas emission boundary (area of boundary ③)-the velocity is quantified in Eq. (24). The estimated gas emission rates are given in Fig. 10. For all three cases, the gas emission rate in Case 1 is lowest and decreases rapidly with time. In Cases 2 and 3, the gas emission rate decreases in early time but the gas emission rates in both cases finally reach stable values. The differences between these three cases can be attributed the differing boundary conditions. In Case 1, there is no gas source from any boundary, which means the cumulative gas emission quantity in this case is absolutely determined by initial

gas contents in the rock-coal blocks - based on the term $q_s = 0$ in Eq. (25). At later times, the gas emission rate will decrease to 0 due to the finite initial gas content. For Cases 2 and 3, there are constant gas sources from the boundaries and theoretically the cumulative gas emission quantities will continuously increase with time. By recalling the gas flow control equation of Eq. (25), q_s is a constant in each case. The gas emission rates in these two cases will show a slightly decreasing trend relative to that of Case 1 at initial time due to the gas content supplements from gas source boundaries. Instead of gas emission rate showing a continuously decreasing trend with a final theoretical value of 0, gas emission rates in these two cases will decrease to constant values. This is due to the gas source boundaries, which is further apparent by comparing the higher gas emission rate in Case 3 to that of Case 2 because Case 3 has an additional gas source boundary (Top roof boundary) for Case 2.

5.4. Numerical model calibration and validation

It is apparent that the transient gas emission rate in each case decreases with time (Fig. 10). Since the gas emission rate from the gob to the face is quantified by integrating the velocity function across the gas emission boundary (area of boundary ③), the
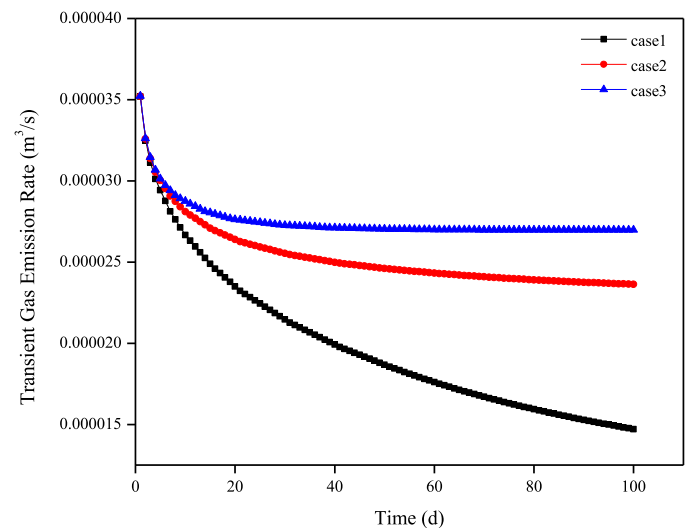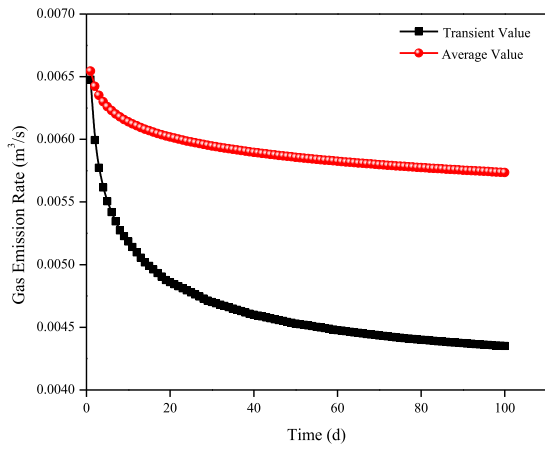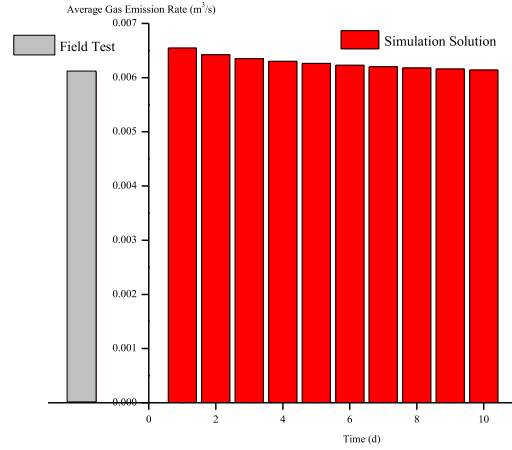

Fig. 10. Curves of gas emission rates for the three cases. In Case 1, gas emission comes solely from the caved rock-coal mass without other gas sources. In Case 2, there is an additional gas source from boundary ① due to the gas influx from top-caved region. In Case 3, there are two additional gas sources from boundary ① and from the top roof boundary ⑥.

(a1)   (a2)

(a) Wide panel
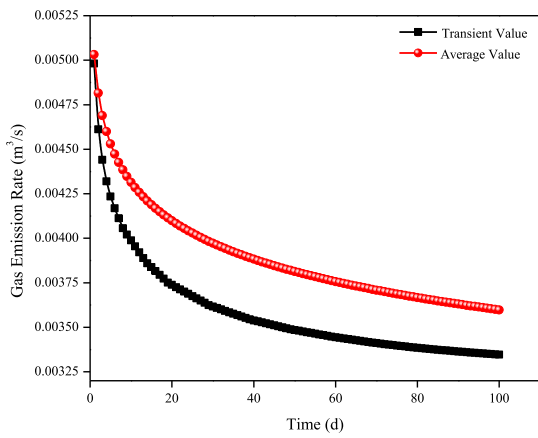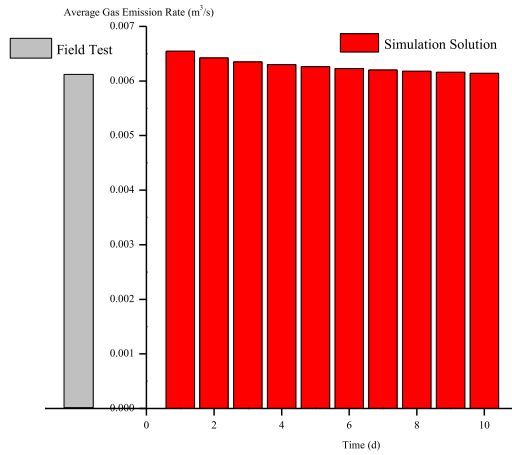
(b1)   (b2)

(b) Transitional-width panel
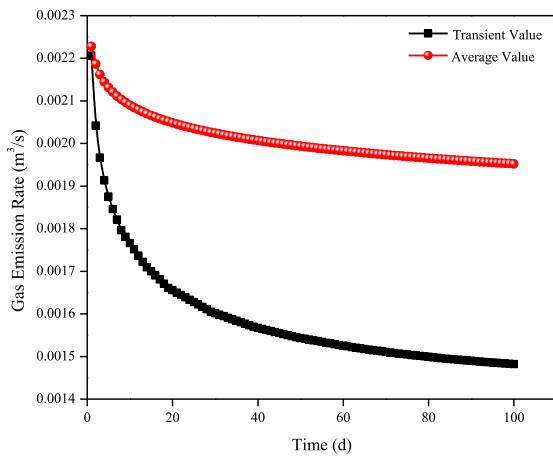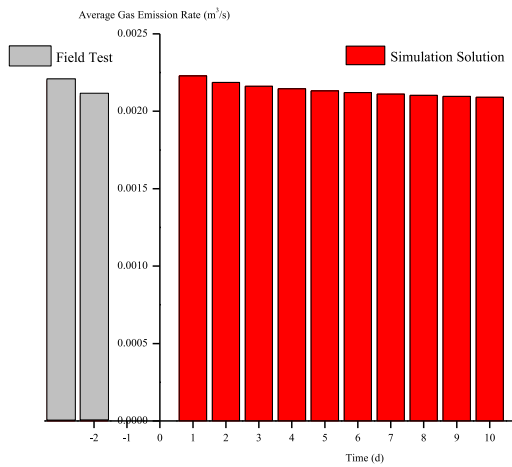
(c1)   (c2)

(c) Narrow panel

Fig. 11. Comparations between simulation solutions and field data. (a) Wide panel. (b) Intermediate-width panel. (c) Narrow panel. (a1), (b1) and (c1) are comparisons between transient and average gas emission rates. (a2), (b2) and (c2) are comparisons between simulation solution and field test data.

transient gas emission rate profile reflects the time-dependent effects of accumulated gas emissions from the gob region (with a gob length of 53 m) to face. In the mine operation, the longwall face continuously retreats and our field monitored data reflect gas emission rate over a particular time period because the survey was conducted along the longwall panel face from headgate to tailgate. The estimated gas emission rate at the face should be an average of the transient gas emission rate during the field investigation time period - this average gas emission rate may be used to validate the modeled results.

The average gas emission rate is quantified by integrating the transient gas emission rate profile over a prescribed time period, mathematically expressed as:

$$q_a = \int_0^t \frac{q_t}{t} dt \qquad (29)$$

where, q_a is the average gas emission rate, m³/s; q_t is the transient gas emission rate, m³/s; and t is the designated time period, d.

For the 6304 working face, the only gas source is from the top-coal caving region and the following simulation solutions are obtained based on Case 2 in Section 5.3. As the 6304 working panel progressively advances at an advance rate of ~ 5 m/d, the newly formed length of the gob is ~50 m in 10 days. In Fig. 11(a1), (b1) and (c1), we estimated the average gas emission rate over 100 days and then use 10day averages of the gas emission to validate the field test data, as illustrated in Fig. 11(a2), (b2) and (c2). This shows that the simulation results agree well with the field investigation data. The results also show that the estimated average gas emission rate over the initial short time period reflect the estimated gas emission rate much better, which implicit that the effects of gob gas emissions from a certain gob length will mainly be reflected by a relative short time period. The reason is that the formation of the gob is synchronous with the progressive advance of the panel advancing. The progressive formation of the new gob region will accumulate and emit gas in the early period when the gob is created. If panel advance is halted, gas emissions from the gob to the face need a relatively long time to develop and should be reflected in the average gas emission rate averaged over a long time period.

6. Discussion

As the mechanical shearer progressively excavates and allows the collapse of the coal, the gob gradually consolidates sufficiently to support a large proportion of the overburden weight [27]. Compacting coal mine gobs are a particularly unique packed bed undergoing dynamic compaction and with an unusually irregular size and shape distribution of rock-coal blocks. The gradually compacted rock-coal behavior results in a reduction in both porosity and the associated permeability of the gob zone. The gob compaction behavior will influence the airflow and the concurrent migration of methane through control variables such as porosity and permeability which will also be reflected in the gob gas emission rate. To evaluate the gas emission intensity from the gob and its interaction with the ventilation systems, a mine-wide ventilation pressure and flow rate survey (p-Q survey) is necessary to establish a ventilation network model.

6.1. Effects of gob compaction behavior on gas emission rate

The challenging conditions of the gob environment make it particularly difficult to conduct direct measurements of porosity and permeability. A few previous studies have quantified these two parameters both experimentally and theoretically [12,23,24,27]. The commonly used cubic law linking permeability and porosity [46–49], allows permeability to be evaluated from the porosity. Thus, we focus on porosity evolution under the influence of size distributions of the rock-coal blocks. Also, the size distributions of the rock-coal blocks both before and after loading must be quantified to simulate gob compaction behavior.

We use a predictive approach [12] that combines fractal scaling in a porous medium with principles of fluid flow. Based on this predictive model, the porosity for a completely fragmented porous medium can be expressed as [12]:

$$\phi = 1 - \left(\frac{\Omega_{min}}{\Omega_{max}} \right)^{3-D_F} \qquad (30)$$
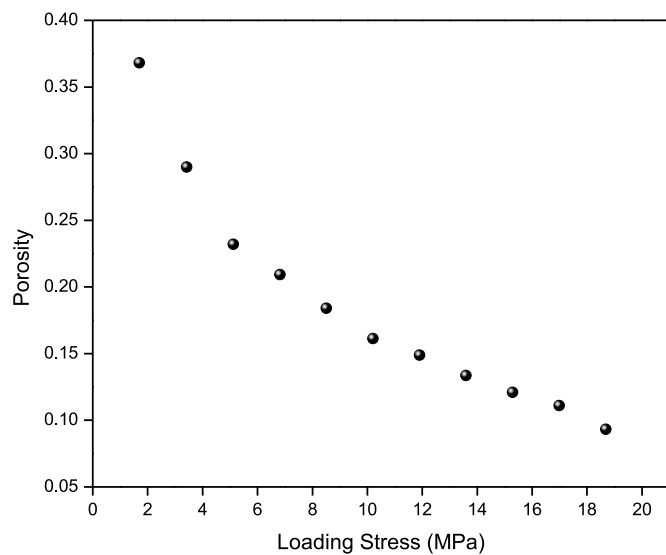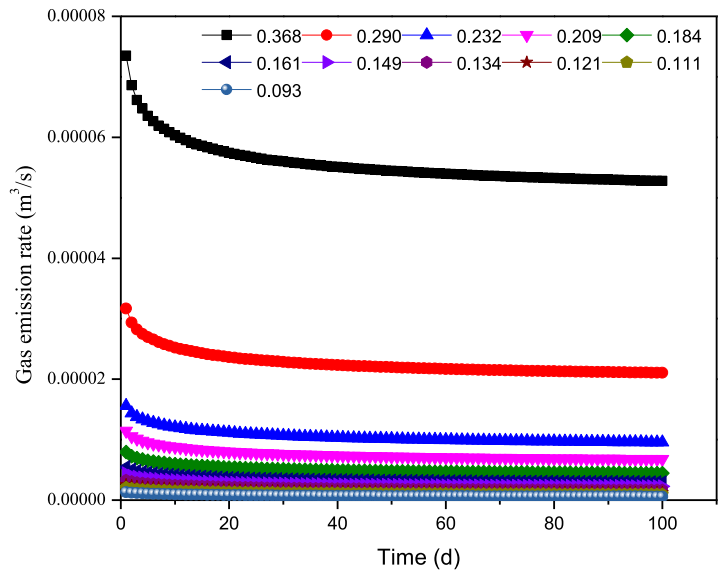
Fig. 12. (a) Porosity evolution of the gob medium when loaded [12]. (b) Effects of porosity evolution on gas emission rates, recovered by inputting porosities from (a) into the numerical model.

Exhausing Ventilation System

13

187.30	187.32
0.0080	

12

10.00	10.01
******	

Leakage Branch of External Air

177.90	177.31
0.0116	

11

106.10	106.09
0.0053	

10

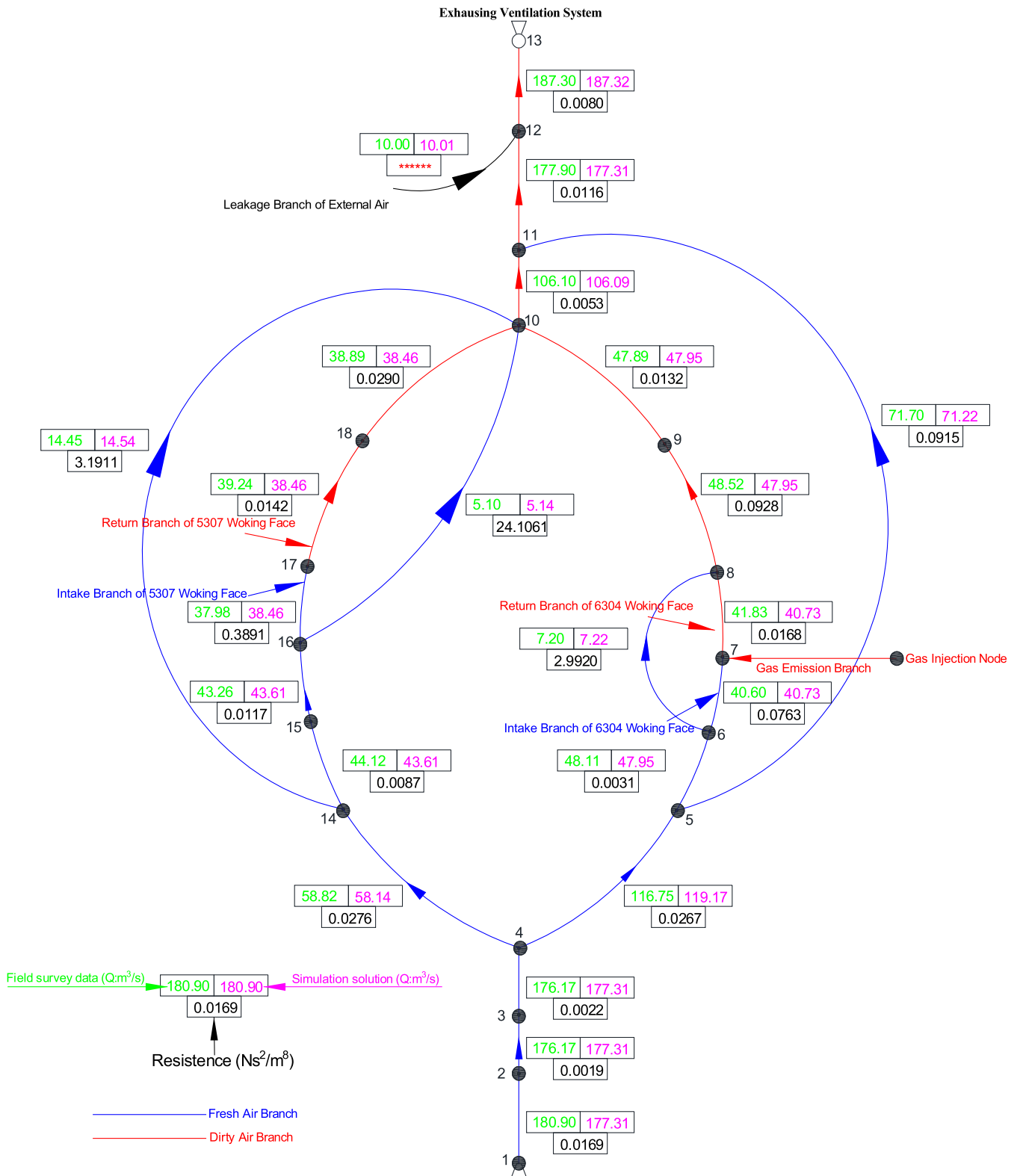| 38.89	38.46
0.0290	

47.89	47.95
0.0132	

18

9

71.70	71.22
0.0915	

14.45	14.54
3.1911	

39.24	38.46
0.0142	

Return Branch of 5307 Woking Face

48.52	47.95
0.0928	

5.10	5.14
24.1061	

17

Intake Branch of 5307 Woking Face

8

Return Branch of 6304 Woking Face

41.83	40.73
0.0168	

37.98	38.46
0.3891	

16

7.20	7.22
2.9920	

7

Gas Injection Node

Gas Emission Branch

43.26	43.61
0.0117	

15

40.60	40.73
0.0763	

Intake Branch of 6304 Woking Face

6

44.12	43.61
0.0087	

48.11	47.95
0.0031	

14

5

58.82	58.14
0.0276	

116.75	119.17
0.0267	

4

Field survey data (Q:m³/s)

180.90	180.90
0.0169	

Simulation solution (Q:m³/s)

Resistence (Ns²/m⁸)

3

176.17	177.31
0.0022	

2

176.17	177.31
0.0019	

180.90	177.31
0.0169	

1

Fresh Air Branch

Dirty Air Branch

Fig. 13. Mine ventilation network modelling and gas injection analyses.

where, ϕ is the total porosity of the fragmented porous medium (dimensionless); Ω_{min} and Ω_{max} are the minimum and maximum particle dimensions (dimensionless); and D_F is the fragmentation fractal dimension (dimensionless).

With an applied stress increment under uniaxial compression, porosity evolution between two successive stress increments can

be expressed as:

$$\phi_{i+1} - \phi_i = -\Lambda \left[\frac{\bar{\sigma}^{\frac{m(D_F-1)}{2}-1}}{\frac{m(D_F-1)}{2}-1} - \frac{\bar{\sigma}_i^{\frac{m(D_F-1)}{2}-1}}{\frac{m(D_F-1)}{2}-1} \right] \qquad (31)$$

where, ϕ_{i+1} and ϕ_i are the porosities under successive one-dimensional applied stresses; $\bar{\sigma}$ and $\bar{\sigma}_i$ are the applied macroscopic stresses (MPa); Λ is the plastic compressibility index (dimensionless); and m is the Weibull modulus (dimensionless).

Based on Eq. (30), the initial porosity is determined by the size distribution of the rock-coal blocks in the gob and the fragmentation fractal dimension. The porosity evolves with an applied increment of one-dimensional applied stress and is quantified by Eq. (30). As shown in Fig. 12(a), the increment in one-dimensional applied stress results in a decrease in porosity, which decrease gas emission rates as the permeability decreases, as illustrated in Fig. 12(b). An eleven-fold increase in stress (1.70–18.68 MPa) results in a nonlinear decrease in porosity of only ~75% (from 0.368 to 0.093) and a 56-fold reduction in gas emission rate (compared to the maximum transient gas emission rate). A sensitivity study was conducted in the numerical modelling to define the evolving porosity (Fig. 12(a)). As shown in Fig. 12 (b), high porosity yields high gas emission rates and low porosity significantly reduces the rate. The size distribution of the rock-coal blocks in the newly formed gob are mainly determined by the failure characteristics of the roof. Normally, large rock blocks fall first, followed by smaller blocks, but the large blocks control the elevated porosity, unless significantly infilled by the smaller fraction (Eq. (30)). The overburden stress builds with time and will compress the rock-coal blocks potentially fracturing the large blocks into a smaller fraction, decreasing the range of block sizes. Thus, the size distribution of rock-coal blocks will become finer in the gob, with time, further resulting to the decrease of pore sizes and potentially also of porosity (based on Eq. (31)).

6.2. Effects of gas emission rate on methane distribution throughout the mine

In order to check the influence of gas emission on the overall methane distribution throughout the mine ventilation network, we conducted mine ventilation network modeling with different gas emission intensities. The Ohioautomation ICAMPS-MineVent software package was selected for the ventilation airflow modeling. The MineVent model allows gas sources to be applied in selected branch(es). This feature was used to investigate the methane concentration distribution throughout the mine ventilation network. The ventilation network model was established to simulate the airflow (Q) distribution for the entire mine as shown in Fig. 13. A mine-wide ventilation pressure and quantity (p-Q) survey was conducted, as described previously. These survey data were used to build the network and the ventilation network was validated by the p-Q survey data. From Fig. 13, it is apparent that the coal mine ventilation system has one intake shaft and one return shaft. Specifically, there were two working faces including the 6304-Face and the 53067-Face during the field investigation periods. Fig. 13 also shows the simulated results of the air quantity (pink numbers). The field-measured and simulated results agree well - suggesting the fidelity of the network model.

This validated model was used as a base model for the gas injection analyses. In Fig. 13, node 7 is the demarcation point between the intake and return entries. The gas emission branch between node 7 and the gas injection node was utilized to address the effects of gas emission on the ventilation network. Several gas emission injection rates into the injection branch were chosen from the simulation solutions including 0.00455 m³/s, 0.00510 m³/s, 0.00546 m³/s, 0.00601 m³/s and 0.00637 m³/s. The ventilation modelling indicates that gas emission from the gob to Face-6304 will not affect its parallel ventilation branch that involves Face-53067. After conducting the gas emission injections, the distributions of methane concentrations at different nodes in the branch involving Face-6304 are shown in Fig. 14. The branch
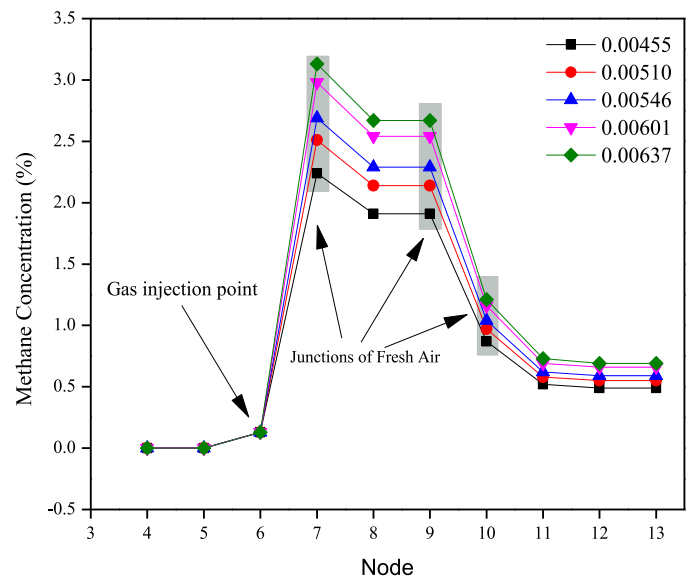

Fig. 14. Effects of different gas emission rates on the ventilation network.

involving Face-6304 includes survey nodes 1, 2, 3, 4, 5, 6, 7, 8, 9, 10, 11, 12 and 13. Among these nodes, nodes from 1 to 6 are located in the intake entry, and nodes from 7 to 13 are located in return entry. Gas emissions occurs at the working face - that is the branch that starts from nodes 6 to 7. As shown in Fig. 14, gas emission has no effect on the intake entry and mainly influence the return entry. In each case, the methane concentration decreases in branch 7-8 (between nodes 7 and 8) due to the junction with the fresh air from branch 6-8 (between nodes 6 and 8) to node 8. Also, branch 9-10 shows a decreasing trend due to supplementary fresh air from branches 14-10 and 16-10. The decrease in methane concentration in branch 10-11 is also attributed to this dilution by fresh air from branches 5-11. Comparing the five cases, if the gas emission quantity increases from 0.00455 m³/s to 0.00637 m³/s, a 50% increase, the peak methane concentration at ventilation node 7 increases by 39.7%, from concentrations of 2.24% to 3.13 %. Based on the mine ventilation network modelling and gas injection analyses, the mine-wide ventilation system is especially sensitive to methane emission rates and these clearly impact methane concentrations in the return branches. In consideration of the explosive limit of methane, in the concentration range of 5-16%, gob gas emission has the potential to trigger elevated methane alarms although all levels remain below the explosive limits.

7. Conclusion

This study provides a systematic method to evaluate gob gas emissions and their interaction with the mine-wide ventilation system. The model incorporates a gas generation and transport model for the gob, idealized as a packed bed and combines this numerical simulation of gas flow within the mine. These models are constrained by field measurements and sued to make predictions of methane concentrations for various plausible and worse case methane emission scenarios. Based on the study, the following major conclusions are drawn:

1) A pressure gradient equation was proposed for gas flow in the rock-coal block medium described as a packed bed. The model describes the gas pressure drop for rock-coal porous medium in the gob, comprising viscous energy losses from the tortuous flow in pore channels as well as the kinetic energy (inertial) losses at the irregular cross-sections.

2) A field campaign of methane monitoring was conducted at the 6304 working face. The measured methane concentration increases monotonically and almost linearly from headgate to tailgate. This finding is anticipated since the methane emitted largely at a uniform rate along the face with this accumulation building along the longwall panel face from headgate to tailgate. The average methane emission rates are estimated as 0.0061 m^3/s for the widest portion of the panel, 0.0044 m^3/s at the transition width, and 0.00215 m^3/s for the narrowest part of the panel, respectively. These estimates rely on and are conditioned by the linearly increasing trend observed from headgate to tailgate.

3) A constitutive model is developed to evaluate gas emission from the gob that couples pressure gradient and diffusive generation and transport mechanisms. This relation was then used to study the case of LTCC mining. The average gas emission rate was defined from the transient gas emission rates based on simulations – which agreed well with field observations.

4) The porosity and effective permeability of the rock-coal block medium is determined by the size distributions of the rock-coal blocks in the gob and the fragmentation fractal dimension, which in turn significantly affects gas emission rates. An increment of applied stress results in a decrease in porosity, which will result in a further decrease in gas emission rate. An eleven-fold increase in stress (1.70–18.68 MPa) results in a nonlinear decrease in porosity of only ∼75% (from 0.368 to 0.093) but a 56-fold reduction on gas emission rate (compared to the maximum transient gas emission rate).

5) A mine-wide ventilation pressure and quantity (p-Q) survey was conducted. The resulting survey data were used to build and constrain the ventilation network modeling.

6) The mine-wide ventilation system is especially sensitive to methane emission rates – a 50% increase in emission rate (from 0.00455 m^3/s to 0.00637 m^3/s) clearly impacts concentrations in the return branches. Peak methane concentration at related branches increase 39.7%, from 2.24% to 3.13% with the potential to trigger elevated methane alarms.

Declaration of Competing Interest

The authors declare no conflict of interest for this manuscript.

CRediT authorship contribution statement

Ang Liu: Writing - original draft. **Shimin Liu:** Supervision. **Gang Wang:** Data curation. **Derek Elsworth:** Software.

Acknowledgement

Supplementary materials

Supplementary material associated with this article can be found, in the online version, at doi:10.1016/j.ijheatmasstransfer.2020.119392.

References

[1] S.S Peng, Coal Mine Ground Control, third ed., Society for Mining, Metallurgy, and Exploration, Englewood, United States, 2008.

[2] J.C. Wang, The Theory and Technique on the Thick Coal Seam Mining, Metallurgical Industry Press, Beijing, 2009.

[3] H. Alehossein, B.A. Poulsen, Stress analysis of longwall top coal caving, Int. J. Rock Mech. Min. Sci. 47 (2010) 30–41.

[4] G.C. Sen, Coal mining in France, Colliery Guard. (1961).

[5] J. Wang, S. Yang, Y. Li, L. Wei, H. Liu, Caving mechanisms of loose top-coal in longwall top-coal caving mining method, Int. J. Rock Mech. Min. Sci. 71 (2014) 160–170.

[6] J. Wold, M.B. Pala, Aspects of Support and Strata Performance on Longwall no.1 at Ellalong Colliery, 1986 CSIRO Division of Geomechnics Report No. 62.

[7] B.A. Poulsen, Evaluation of Software Code UDEC for Modelling Top Coal Caving in an Australian Environment, 2003 CSIRO Exploration and Mining Report 1115F.

[8] G.X. Xie, J.C. Chang, K. Yang, Investigations into stress shell characteristics of surrounding rock in fully mechanized top-coal caving face, Int. J. Rock Mech. Min. Sci. 46 (2009) 172–181.

[9] H. Xie, Z. Chen, J. Wang, Three-dimensional numerical analysis of deformation and failure during top coal caving, Int. J. Rock Mech. Min. Sci. 36 (1999) 651–658.

[10] N.E. Yasitli, B. Unver, 3D numerical modeling of longwall mining with top-coal caving, Int. J. Rock Mech. Min. Sci. 42 (2005) 219–235.

[11] L. Fan, S. Liu, A conceptual model to characterize and model compaction behavior and permeability evolution of broken rock mass in coal mine gobs, Int. J. Coal Geol. 172 (2017) 60–70.

[12] C.Ö. Karacan, Prediction of porosity and permeability of caved zone in longwall gobs, Transp. Porous Media. 82 (2010) 413–439.

[13] R.B. Krog, S.J. Schatzel, F. Garcia, J.K. Marshall, Predicting methane emissions from longer longwall faces by analysis of emission contributors, in: Proc. 11th U.S./North Am. Mine Vent. Symp. - 11th U.S./North Am. Mine Vent. Symp, 2006, 2006, pp. 383–392.

[14] C.Ö. Karacan, A new method to calculate permeability of gob for air leakage calculations and for improvements in methane control, in: Proc. 13th U.S./North Am. Mine Vent. Symp, 2010.

[15] C.Ö.L. Karacan, Stochastic modeling of gob gas venthole production performances in active and completed longwall panels of coal mines, Int. J. Coal Geol. 84 (2010) 125–140.

[16] S. McAteer, J.D. Beall, K. Beck, J.A. McGinley, P.C. Monforton, C. Roberts, D.C. Spence, B. Weise, Explosive: a Failure of Basic Coal Mine Safety Practices, 2010, p. 121. . Report to the Governor, Governor's Independent Investigation panel, May.

[17] A.D.S. Gillies, Coal mine face area ventilation, ventilation of coal mines, in: Proceedings of the symposium, Australasian Inst of Mining & Metallurgy, Wollongong, Illawarra Branch, 1983.

[18] M.T. Parra, J.M. Villafruela, F. Castro, C. Méndez, Numerical and experimental analysis of different ventilation systems in deep mines, Build. Environ 41 (2006) 87–93.

[19] J. Cheng, S. Yang, Data mining applications in evaluating mine ventilation system, Saf. Sci. 50 (2012) 918–922.

[20] K.A. El-Nagdy, Stability of multiple fans in mine ventilation networks, Int. J. Min. Sci. Technol. 23 (2013) 569–571.

[21] B.P. Kazakov, A.V. Shalimov, M.A. Semin, Stability of natural ventilation mode after main fan stoppage, Int. J. Heat Mass Transf. 86 (2015) 288–293.

[22] K. Wang, Z. Wu, A. Zhou, Y. Jiang, S. Feng, Experimental study of high concentrations of coal mine methane behavior in downward ventilated tilted roadways, J. Wind Eng. Ind. Aerodyn. 158 (2016) 69–80.

[23] C.Ö. Karacan, G.S. Esterhuizen, S.J. Schatzel, W.P. Diamond, Reservoir simulation-based modeling for characterizing longwall methane emissions and gob gas venthole production, Int. J. Coal Geol. 71 (2007) 225–245.

[24] D.J. Brunner, Ventilation models for longwall leakage simulation, in: 2nd US Mine Ventilation Symposium, Reno,NV, 1985, pp. 23–25.

[25] G.S. Esterhuizen, C.O. Karacan, Development of numerical models to investigate permeability changes and gas emission around longwall mining panel, the Alaska Rocks, in: 40th US Symposium on Rock Mechanics, Anchorage, Alaska, 2005, pp. 25–26. June.

[26] C. Zhang, S. Tu, L. Zhang, Q. Bai, Y. Yuan, F. Wang, A methodology for determining the evolution law of gob permeability and its distributions in longwall coal mines, J. Geophys. Eng. 13 (2016) 181–193.

[27] C. Pappas, D.M., Mark, Behavior of SIMUlated Longwall Gob Material, Report of Investigations RI No. 9458, US Department of Interior, US Bureau of Mines.

[28] R.R. Jozefowicz, The Post-Failure Stress-Permeability Behaviour of Coal Measure Rocks, University of Nottingham, 1997.

[29] G.S. Esterhuizen, C.Ö. Karacan, A methodology for determining gob permeability distributions and its application to reservoir modeling of coal mine longwalls, SME Annu. Meet. Exhib. (2007) 6.

[30] S. Ergun, A.A. Orning, Fluid flow through randomly packed columns and fluidized beds, Ind. Eng. Chem. 41 (1949) 1179–1184.

[31] K. Vafai, C.L. Tien, Boundary and inertia effects on flow and heat transfer in porous media, Int. J. Heat Mass Transf. 24 (1981) 195–203.

[32] Y. Demirel, R. Kahraman, Thermodynamic analysis of convective heat transfer in an annular packed bed, Int. J. Heat Fluid Flow 21 (2000) 442–448.

[33] A.R.A. Khaled, K. Vafai, The role of porous media in modeling flow and heat transfer in biological tissues, Int. J. Heat Mass Transf. 46 (2003) 4989–5003.

[34] R.E. Hicks, Pressure drop in packed beds of spheres, Ind. Eng. Chem. Fund. 9 (1970) 500–502.

[35] R.K. Niven, Physical insight into the Ergun and Wen and Yu equations for fluid flow in packed and fluidised beds, Chem. Eng. Sci. 57 (2002) 527–534.

[36] J. Wu, B. Yu, M. Yun, A resistance model for flow through porous media, Transp. Porous Media 71 (2008) 331–343.

[37] K. Wang, A. Liu, A.T. Zhou, International Journal of Mining Science and Technology Theoretical analysis of influencing factors on resistance in the process of gas migration in coal seams, Int. J. Min. Sci. Technol. 27 (2017) 315–319.

[38] S. Ergun, Fluid flow through packed columns, Chem. Eng. Prog. (1952).

[39] E.N. Bird, R.B. Stewart, W.E. Lightfoot, Transport Phenomena, Chap 6., Wiley, New York, 1960.

[40] Y. Zhang, Fluid Mechanics, Chap (3, 6), Higher Education Press, 1999.

[41] A. Saghafi, M. Faiz, D. Roberts, CO_2 storage and gas diffusivity properties of coals from Sydney Basin, Australia, Int. J. Coal Geol. 70 (2007) 240–254.

[42] J. Liu, Z. Chen, D. Elsworth, X. Miao, X. Mao, Evaluation of stress-controlled coal swelling processes, Int. J. Coal Geol. 83 (2010) 446–455.

[43] I. Langmuir, The constitution and fundamental properties of solids and liquids. II. Liquids, J. Am. Chem. Soc. 39 (1917) 1848–1906.

[44] J.Q. Shi, S. Durucan, M. Fujioka, A reservoir simulation study of CO2injection and N2flooding at the Ishikari coalfield CO_2 storage pilot project, Japan,, Int. J. Greenh. Gas Control 2 (2008) 47–57.

[45] D. Chen, Z. Pan, J. Liu, L.D. Connell, An improved relative permeability model for coal reservoirs, Int. J. Coal Geol 109-110 (2013) 45–57.

[46] M. Palmer, How permeability depends on stress and pore pressure in coalbeds: a new model, SPE Reserv. Eval. Eng. (1998) 539–544.

[47] S. Liu, S. Harpalani, Permeability prediction of coalbed methane reservoirs during primary depletion, Int. J. Coal Geol. 113 (2013) 1–10.

[48] S. Liu, S. Harpalani, Determination of the effective stress law for deformation in coalbed methane reservoirs, Rock Mech. Rock Eng. 47 (2014) 1809–1820.

[49] S. Liu, S. Harpalani, Compressibility of sorptive porous media: Part 1. Background ana theory, Am. Assoc. Pet. Geol. Bull. 98 (2014) 1761–1772.

[50] B. Abbasi, Y.P. Chugh, H. Gurley, An analysis of the possible fault displacements associated with a retreating longwall face in Illinois, in: 48th U.S. Rock Mechanics/Geomechanics Symposium, 1-4 June, Minneapolis, Minnesota, 2014.